

# A Cosmic Double Helix in the Archetypical Quasar 3C273

A. P. Lobanov<sup>1\*</sup> and J. A. Zensus<sup>1,2</sup>

Finding direct evidence for plasma instability in extragalactic jets is crucial for understanding the nature of relativistic outflows from active galactic nuclei. Our radio interferometric observations of the quasar 3C273 made with the orbiting radio telescope, HALCA, and an array of ground telescopes have yielded an image in which the emission across the jet is resolved, revealing two threadlike patterns that form a double helix inside the jet. This double helical structure is consistent with a Kelvin-Helmholtz instability, and at least five different instability modes can be identified and modeled by a light jet with a Lorentz factor of 2 and Mach number of 3.5. The model reproduces in detail the internal structure of the jet on scales of up to 30 milli-arc seconds ( $\sim 300$  parsecs) and is consistent with the general morphology of the jet on scales of up to 1 kiloparsec.

One of the most intriguing features observed in active galactic nuclei (AGN) is highly collimated, relativistic plasma outflows (jets) that originate in the immediate vicinity of the center of activity and propagate at distances of up to several Mpc (1 pc = 3.26 light-years =  $3.08 \times 10^{18}$  cm). Observations of jets in AGN probe the behavior of extremely relativistic matter in the universe and provide a unique, remote “laboratory” for studying the most powerful cosmic phenomena such as supermassive black holes and extragalactic accretion disks. The quasar 3C273 (1) is one of the closest, most luminous, and best studied AGN (2), with a prominent, relativistic outflow observed in the x-ray (3, 4), optical (5), and radio (6–10) wave bands. The relativistic jet observed in the quasar 3C273 is one-sided, with no signs of emission on the counterjet side at dynamic ranges of up to 16,000:1 (10). This is evidence for strong relativistic boosting in an intrinsically double-sided outflow powered by an accretion disk around a central black hole (11). The enhanced emission features (jet components) identified in the jet on scales of up to  $\sim 20$  milli-arc seconds (mas) are moving at apparent speeds exceeding the speed of light by factors of 5 to 8 (12). The position angle at which they are ejected shows regular variations with a likely period of about 13 to 15 years (13). These jet components may result from the flares observed in 3C273 in the optical (14) and radio (15) wavelengths and also reflect the precession of the jet axis (13). The structure and kinematics of such outflows are typically explained in terms of

shock waves (16–20) and Kelvin-Helmholtz (K-H) instability (21–25).

Recent studies have shown that the instability may produce complex, three-dimensional ribbonlike and threadlike patterns inside a relativistic jet (25). In these ribbons and threads, an order of magnitude increase of particle density and radio emissivity can be expected. In view of these findings, observational studies of internal structure of parsec-scale jets become particularly important for understanding the role of plasma instabilities in relativistic flows. Such studies require observations at extremely high angular resolution, which can be satisfied at present only by radio wavelength observations with very long baseline interferometry (VLBI) (26). In VLBI, the image fidelity and noise level are determined, to the first order, by the number and configuration of participating radio telescopes. The corresponding image resolution is  $\propto \lambda/D_1$ , where  $\lambda$  is the observing wavelength and  $D_1$  is the longest of the baselines between the participating telescopes. The space VLBI mission VSOP (VLBI Space Observatory Programme) (27, 28), led by the Japanese Institute of Space and Astronautical Science, has complemented ground VLBI arrays with an orbiting 8-m antenna on board of the satellite HALCA (29). The VSOP observations provide three to four times better resolution, compared with ground VLBI observations at similar frequencies. For relatively close AGN, the resolution of the VSOP is sufficient for resolving the internal structure of their jets. We present here the analysis of a VSOP image of radio emission at  $\lambda = 6$  cm from the parsec-scale jet in 3C273. The VSOP observation of 3C273 was supported by 10 VLBA (30) antennae and the Effelsberg 100-m telescope (31). The data reduction and other specific details of the observation have been discussed elsewhere (32, 33).

The VSOP image of 3C273 (Fig. 1) has

the formal dynamic range of 2100:1. The image reveals the internal structure of the jet, benefiting from the favorable orientations of the space baselines, which provide a 0.7-mas resolution in the direction perpendicular to the jet axis. At the redshift of 3C273 [ $z = 0.158$  (34)], this corresponds to a linear scale of 1.7 pc (for the standard cosmology with the Hubble constant,  $H_0 = 70 \text{ km s}^{-1} \text{ Mpc}^{-1}$  and deceleration parameter,  $q_0 = 0.5$ ). The complexity of the emission distribution across the jet is visible in the profiles (inset of Fig. 1). Extensive tests of the fidelity of the imaging algorithm allow us to conclude that the incompleteness of the spatial sampling of our VSOP data becomes an insignificant factor at flux density levels above 6 mJy/beam. With this estimate, the most conservative limit on the dynamic range of the image is about 700:1, which is sufficient for the purposes of studying the emission distribution along, and across, the jet. To determine the interior structure of the jet, we obtained 240 profiles of brightness distribution across the jet. All of the profiles are centered on the smoothed ridge line of the jet (Fig. 1). Each profile is oriented orthogonally to the local direction of the ridge line. The centers of adjacent profiles are separated by 0.1 mas, which provides sufficient redundancy of the measurements. In most of the profiles, the presence of at least two distinct features is visible (35). We fit each profile by two Gaussians (Gaussian components) and determine their positions, amplitudes, and widths. We designate the two Gaussian components as P1 and P2 (Fig. 1). The two components can be distinguished from each other by their size and strength, with the component P1 being typically stronger and more compact than P2. For all of the fits, we find that the mean residuals after the fitting are within 6 mJy and the largest residual amplitudes do not exceed 15 mJy. These levels are smaller than the amplitudes measured in all of the profiles.

The threads P1 and P2 (Fig. 1) form a regular pattern, resembling a double helix. The presence of such a pattern indicates a K-H instability developing in an outflow that has transverse velocity gradients or discontinuities due to interaction between the flowing relativistic plasma and (typically) subrelativistic surrounding material. In such a case, the locations of P1 and P2 inside the jet will be determined by the relative strengths of the most prominent modes of the instability. The spatial and temporal evolution of different modes of K-H instability depends ultimately on the plasma speeds and Mach numbers in the flow itself ( $\beta_j, M_j$ ) and in the surrounding medium ( $\beta_x, M_x$ ), as well as on the ratio,  $\eta = \rho_j/\rho_x$ , between the densities in the flow and the surrounding medium. Formation of an instability depends on the presence of an external periodic process (such as precession

<sup>1</sup>Max-Planck-Institut für Radioastronomie, Auf dem Hügel 69, 53121 Bonn, Germany. <sup>2</sup>National Radio Astronomy Observatory, 520 Edgemont Road, Charlottesville, VA 22903, USA.

\*To whom correspondence should be addressed. E-mail: alobanov@mpifr-bonn.mpg.de

REPORTS

of the jet axis, rotation of the accretion disk, or motion of the base of the jet) providing the initial perturbation of the jet plasma and driving the basic instability modes. Propagation and growth or damping of individual instability modes can be described by the dispersion relation constructed for a random, linear perturbation,  $\epsilon(\rho, v, P)$ , of the jet density  $\rho$ , velocity  $v$ , and pressure  $P$  (21–24). Each mode of the instability is characterized by one longitudinal ( $k$ ) and two azimuthal ( $n, m$ ) wave numbers. The latter two numbers determine the wavelength of a mode and whether the corresponding perturbation affects the surface ( $m = 0$ ) or the interior ( $m > 0$ ) of the jet. The pinch ( $n = 0$ ), helical ( $n = 1$ ), and elliptical ( $n = 2$ ) modes are expected to be most prominent in supersonic, relativistic flows (24, 25). Each mode reaches the maximum growth rate at its respective resonant wavelength,  $\lambda_{nm}^*$ . The body modes are effectively damped at wavelengths larger than the longest unstable wavelength,  $\lambda_{nm}^1 \lesssim 2\lambda_{nm}^*$ . The surface modes do not have the longest unstable wavelength, and they can be driven externally at arbitrarily long wavelengths. Several modes of K-H instability may be operating simultaneously in a jet, modulating, and interacting with each other. For such a case, the wavelengths (and to a lesser extent, also the phases and amplitudes) of surviving modes in the jet in 3C273 can be recovered from fitting the observed positions of the threads P1 and P2 by a number of generic sinusoidal modes with amplitude growth and damping terms incorporated.

We approximate the positions of the threads P1 and P2 by the sum of several sinusoidal modes and determine their wavelengths, phases, and amplitudes (36). Each individual sinusoidal mode,  $r_i$ , is described by a set of four parameters: wavelength  $\lambda_i$ , phase  $\psi_i$ , maximum amplitude  $a_i$ , and distance  $z_i$  at which the maximum amplitude is reached (37). We find that five modes are required to represent the positions of P1 and P2 (Fig. 2 and Table 1). The parameters of the fitted modes are correlated (Table 1). The first two fitted modes of P1 are identical to the respective modes of P2. Modes 4 and 5 of P1 differ only in their phases from the respective modes of P2. The offset between the respective phases of the third, fourth, and fifth modes of P1 and P2 is  $180^\circ$ . In addition to that, the third and fourth modes in each thread are also offset by  $180^\circ$  from each other. Preserving these phase offsets is needed to fit the observations: Changing any of them by as much as  $5^\circ$  degrades the goodness of the fit ( $\chi^2$  parameter) by a factor of 2.5. Another critical condition is the closeness of the wavelengths of the third and fourth modes in both threads. No good fit can be achieved whenever the relative ratio of these wavelengths is increased by more than 10% (im-

plying that the third and fourth modes must not interfere destructively with each other). These relations between different modes reduce the effective number of free parameters to 16, providing an additional assurance that the fits are not overdetermined. We conclude therefore that P1 and P2 must be produced by essentially the same set of five sinusoidal

modes. The first and second fitted modes may represent two different surface modes of K-H instability [because the surface modes should have the same effect on both threads (25)]. The other three fitted modes may correspond to the body modes of the instability [thus producing two threads inside the jet propagating with a  $180^\circ$  phase offset (25)].

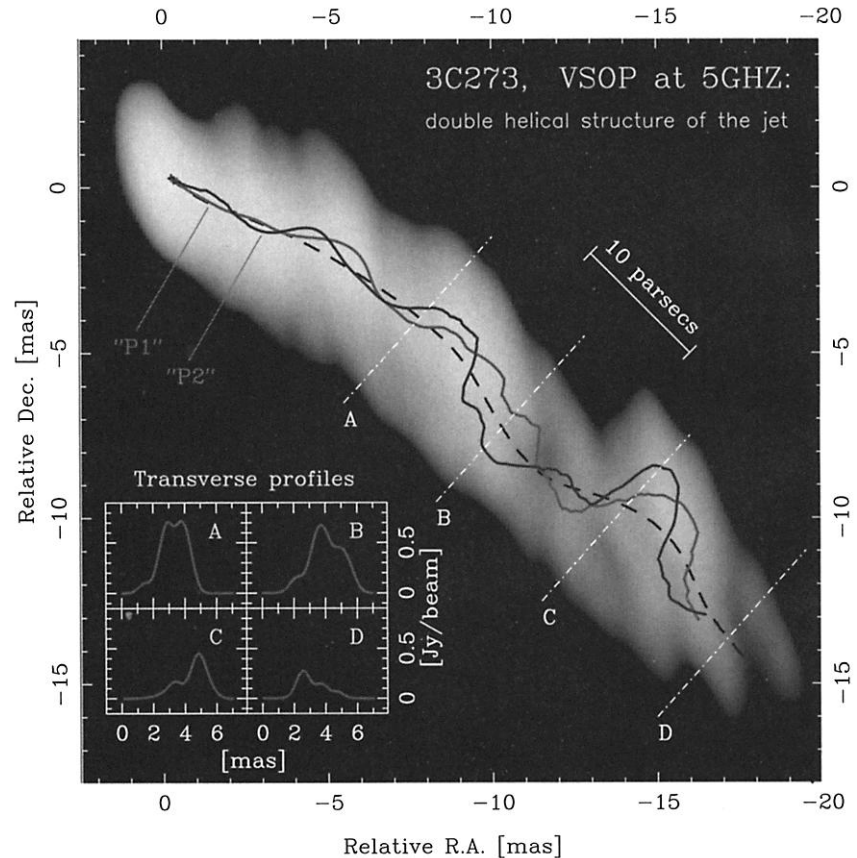


**Fig. 1.** Parsec-scale radio jet in 3C273 imaged at 5 GHz by the VSOP. The image is restored with a Gaussian point-spread function (beam), which has major and minor axes of 2.1 mas and 0.5 mas, oriented at a position angle of  $12.9^\circ$ . The peak brightness in the image is 4.52 Jy/beam ( $\text{Jy} = \text{jansky} = 10^{-23} \text{ erg cm}^{-2} \text{ s}^{-1} \text{ Hz}^{-1}$ ), and the noise level is  $\sigma = 2.1 \text{ mJy/beam}$ . The dot-dashed white lines denote the locations of the four flux density profiles shown in the inset. A total of 240 such profiles have been measured along the jet. Each of these profiles is centered on the smoothed ridge line (the dashed black line) and oriented orthogonally to it. Each of the measured profiles is fitted by two Gaussian components designated as P1 and P2. The locations of the peaks of P1 and P2 are marked in the image by the light gray and dark gray lines. The double helical pattern formed by P1 and P2 suggests that they result from K-H instability developing in the jet. Dec., declination; R.A., right ascension.

**Table 1.** Measured parameters of the modes contributing to P1 and P2. Columns of the table represent the following: Mode, mode number;  $\lambda_i$ , fitted wavelength;  $a_i$ , amplitude;  $\phi_i$ , phase;  $z_i$ , peak distance; K-H mode, K-H mode identified with the fitted wavelength;  $\epsilon_{\lambda_i}$ , discrepancy between the measured and theoretical wavelength of the corresponding K-H mode; and  $\lambda^*$ , characteristic wavelength.

Mode	$\lambda_i$ (mas)		$a_i$ (mas)		$\phi_i$ (deg)		$z_i$ mas		K-H mode	$\epsilon_{\lambda_i}$	$\lambda^*$ (mas)
	P1	P2	P1	P2	P1	P2	P1	P2			
1	18.0		1.5		180		40		$H_s$		27.0
2	12.0		1.4		260		40		$E_s^*$	7%	15.0
3	3.9	4.1	2.2	1.5	315	135	20		$H_{b1}^*$	4%	14.4
4	3.8		1.2		135	315	20		$E_{b1}^*$	15%	16.0
5	1.9		0.25		175	355	20		$E_{b2}^*$	10%	12.4

**Table 2.** Kelvin-Helmholtz instability model for the jet in 3C273.

Model parameters			Model predictions			Measurements	
Lorentz factor	$\Gamma_j$	$2.1 \pm 0.4$	Mode	$\lambda_{n,m}^*$ [mas]	$\lambda_{n,m}^\dagger$ [mas]	$\lambda_j$ [mas]	Identification
Mach number	$M_j$	$3.5 \pm 1.4$					
Density ratio	$\eta$	$0.023 \pm 0.012$	$H_s^\ddagger$	$9.8 \pm 2.3$	$18.0 \pm 4.6$	18.0	Positive§
Jet radius (pc)	$R_j$	$0.8 \pm 0.2$	$H_{b1}^\ddagger$	$4.2 \pm 1.0$	$7.7 \pm 1.9$	3.9–4.1	Positive
Jet half-opening angle	$\phi_j$	$15^\circ \pm 0.2^\circ$	$H_{b2}^\ddagger$	$2.7 \pm 0.6$	$4.3 \pm 1.0$	–	Damped?
Jet viewing angle	$\theta_j$	$15^\circ \pm 3^\circ$	$H_{b3}^\ddagger$	$1.9 \pm 0.5$	$2.9 \pm 0.7$	1.9†	Probable
<i>Calculated jet properties</i>			$E_s^\ddagger$	$11.9 \pm 2.8$	–	12.0	Positive
Jet sound speed	$a_j$	$0.53 \pm 0.16$	$E_{b1}^\ddagger$	$3.3 \pm 0.8$	$5.5 \pm 1.3$	3.8	Positive
Ambient medium sound speed	$a_x$	$0.08 \pm 0.03$	$E_{b2}^\ddagger$	$2.3 \pm 0.5$	$3.5 \pm 0.8$	1.9†	Positive
Instability propagation speed	$v_w$	$0.21 \pm 0.06$	$E_{b3}^\ddagger$	$1.7 \pm 0.4$	$2.6 \pm 0.6$	1.9†	Probable

†Modes most likely present in the jet. ‡Possible multiple modes acting together. §Externally driven mode.

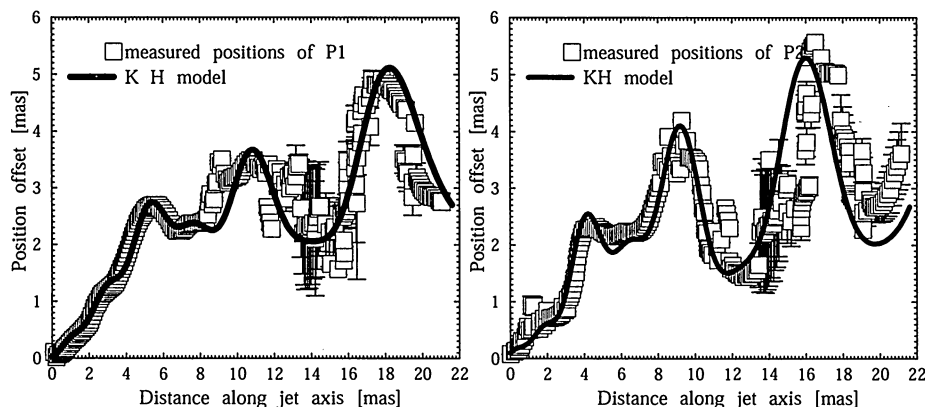


**Fig. 2.** The positions of P1 (left) and P2 (right) fitted by a model of K-H instabilities propagating in the jet. The reduced  $\chi^2$  parameters of the fits are 1.4 and 2.5, respectively. The parameters of the contributing instability modes are listed in Table 1. At distances  $\geq 12$  mas ( $\geq 120$  pc), the model deviates from the observed positions because of a likely deflection of the jet caused by its interaction with the interstellar medium. The deflection angle required to explain the discrepancy is  $\approx 2^\circ$ .

The correspondence between the fitted modes and the modes of K-H instability can be described by the characteristic wavelength,  $\lambda^* = \lambda_i(n_i + 2m_i + 1/2)$ , where  $n_i$  and  $m_i$  are the azimuthal wave numbers of the instability mode identified with the measured wavelength  $\lambda_i$ . The characteristic wavelength depends only on the physical conditions in the jet (expressed by  $\beta_j$ ,  $M_j$ , and  $\eta$ ), and therefore it must be the same for all of the fitted modes (38). We applied this criterion for testing various possible mode identifications and found that the fitted modes admit only one physically plausible combination of K-H instability modes (Table 1). The modes 2 through 5 must grow at their resonant wavelengths, with the corresponding average  $\lambda_{[2-5]}^* = 14.5 \pm 3.1$ . The much larger  $\lambda^*$  of the first mode indicates that the helical surface mode must be driven externally (the alternative would be to assume a  $>10$  mas error in the fitted wavelength, which is improbable). The driving mechanism for the  $H_s$  mode can be associated with the 15-year period suggested from the observed changes of the ejection angle in the jet of 3C273 (13).

To model the observed modes, we assume that the jet has a conical shape with radius  $R_j$

measured at the jet origin and a small opening half-angle  $\phi_j \ll 1/M_j$  [ensuring that the evolution of K-H instability is well approximated by the solutions obtained for a linear perturbation in a cylindrical jet (22, 23, 25)]. The jet flow is directed at an angle  $\theta_j$  with respect to the line of sight, and the jet plasma moves at a speed characterized by a Lorentz factor  $\Gamma_j = (1 - \beta_j^2/c^2)^{-1/2}$ . These assumptions are sufficient for estimating the resonant and longest unstable wavelengths (24) of different modes of a K-H instability (taking into account the propagation speed,  $v_w$ , of the instability). An additional constraint is given by the driving period  $P_o = 15$  years, which we associate with the  $H_s$  mode. The physical parameters of the jet derived under these assumptions (Table 2) provide a description of the measured wavelengths and satisfy the observed  $P_o$  (39). The errors of the model parameters and derived jet properties are 1 $\sigma$  deviations determined from  $\chi^2$  parameter of the fit.

For all of the identified instability modes, the predicted and measured wavelengths agree within the formal errors of the model (Table 2). The model provides a self-consistent explanation for the correlations found in the fitted

modes identified with several modes of K-H instability. The model also explains in detail the internal structure of the jet on scales  $\geq 30$  mas ( $\geq 300$  pc), accommodates the general morphology of the jet on scales of  $\geq 100$  mas ( $\geq 1$  kpc), and accounts for the observed periodic changes of the jet ejection angle. We conclude that the instability in the jet of 3C273 is developing in a plasma with moderate Lorentz factor and Mach number and a much lower density than that of the surrounding material. The calculated sound speeds agree with the values expected for a light, electron-positron jet plasma and a subrelativistic ambient medium. The derived  $\Gamma_j = 2.1$  corresponds to an apparent speed  $\beta_{app} = \beta_j \sin \theta_j / (1 - \beta_j \cos \theta_j) = 1.4c$ , which is lower than the apparent speeds of 5 to  $8c$  typically measured in the jet of 3C273 (12). However, the apparent speeds are determined from the motions of enhanced emission features that are probably associated with relativistic shock waves inside the jet. The bulk Lorentz factor of these features can be much higher than the Lorentz factor of the underlying flow. In contrast to this, the speed inferred from fitting the positions of the threads P1 and P2 reflects the speed of the slower, underlying flow in which the instability develops. This implies that there should be a substantial velocity gradient across the jet.

#### References and Notes

1. M. Schmidt, *Nature* **197**, 1040 (1963).
2. T. J.-L. Courvoisier, *Astron. Astrophys. Rev.* **9**, 1 (1998).
3. R. M. Sambruna *et al.*, *Astrophys. J.* **549**, L161 (2001).
4. H. L. Marshall *et al.*, *Astrophys. J.* **549**, L167 (2001).
5. R. C. Thompson, C. D. Mackay, A. E. Wright, *Nature* **365**, 133 (1993).
6. T. J. Pearson *et al.*, *Nature* **290**, 365 (1981).
7. J. A. Zensus, L. B. Bååth, M. H. Cohen, G. D. Nicolson, *Nature* **334**, 410 (1988).
8. R. G. Conway, S. T. Garrington, R. Perley, J. A. Biretta, *Astron. Astrophys.* **267**, 347 (1993).
9. R. J. Davis, S. C. Unwin, T. W. B. Muxlow, *Nature* **354**, 374 (1991).
10. S. C. Unwin *et al.*, *Astrophys. J.* **280**, 109 (1985).
11. M. C. Begelman, R. D. Blandford, M. J. Rees, *Rev. Mod. Phys.* **56**, 255 (1984).
12. Z. Abraham, E. Carrara, J. A. Zensus, S. C. Unwin, *Astron. Astrophys. Suppl.* **115**, 543 (1996).
13. Z. Abraham, G. E. Romero, *Astron. Astrophys.* **344**, 61 (1999).
14. M. K. Babadzhanyants, E. T. Belokon', *Astron. Zh.* **70**, 241 (1993).

15. M. Türlér, T. J.-L. Courvoisier, S. Paltani, *Astron. Astrophys.* **349**, 45 (1999).
16. A. P. Marscher, *Astrophys. J.* **235**, 386 (1980).
17. J. L. Gómez, A. Alberdi, J. M. Marcaide, *Astron. Astrophys.* **274**, 55 (1993).
18. ———, *Astron. Astrophys.* **284**, 51 (1994).
19. J. L. Gómez, A. Alberdi, J. M. Marcaide, A. P. Marscher, J. P. Travis, *Astron. Astrophys.* **292**, 33 (1994).
20. A. J. Mioduszewski, P. A. Hughes, D. G. Comer, *Astrophys. J.* **476**, 649 (1997).
21. P. E. Hardee, *Astrophys. J.* **287**, 523 (1984).
22. ———, *Astrophys. J.* **303**, 111 (1986).
23. ———, *Astrophys. J.* **313**, 607 (1987).
24. ———, D. A. Clarke, A. Rosen, *Astrophys. J.* **485**, 533 (1997).
25. P. E. Hardee, *Astrophys. J.* **533**, 176 (2000).
26. J. A. Zensus, P. D. Diamond, P. J. Napier, Eds., *Very Long Baseline Interferometry and the VLBA, ASP Conference Series*, vol. 82 (Astronomical Society of the Pacific, San Francisco, 1995).
27. H. Hirabayashi et al., *Science* **281**, 1825 (1998).
28. H. Hirabayashi et al., *Publ. Astron. Soc. Jpn.* **52**, 955 (2000).
29. HALCA is the Highly Advanced Laboratory for Communications and Astronomy.
30. The Very Long Baseline Array is operated by the National Radio Astronomy Observatory, USA.
31. The Effelsberg 100-m telescope is operated by Max-Planck-Institut für Radioastronomie, Bonn, Germany.
32. A. P. Lobanov et al., *Adv. Space Res.* **26**, 669 (2000).
33. A. P. Lobanov, T. P. Krichbaum, A. Witzel, J. A. Zensus, *New Astron. Rev.* **43**, 741 (1999).
34. M. A. Strauss et al., *Astrophys. J. Suppl.* **83**, 29 (1992).
35. At distances from the jet origin larger than 12 mas, the profiles show evidence for even more complex structure, with perhaps a third, weaker and more extended emitting component inside the jet (as seen, for instance, in the profile "D" plotted in the inset of Fig. 1). The spatial sampling of the VSOP data does not permit us to determine unambiguously the peak and the size of such extended features, and this limits our present study to measuring the properties of the two stronger features inside the jet.
36. The position offsets of the threads P1 and P2 are first calculated with respect to a fixed jet axis, and then a precession term is introduced. The position angle of the jet axis,  $\Phi_j = -138^\circ$ , is estimated from the available images of kiloparsec-scale structures in 3C273 (8). The precession wavelength,  $\lambda_{\text{prec}} = 100 \pm 20$  mas, is estimated from high dynamic range VLBI images of 3C273 (10). With the precession term applied, we proceed to determine the minimum number of sinusoidal modes necessary to represent the observed locations of the threads P1 and P2.
37. The evolution of a sinusoidal mode is described by an amplitude term  $G(z) = a_i(2ze^{-z/z_i})/(z+z_i)$ , where  $z$  is the coordinate along the jet axis. The corresponding position offset introduced by the mode in the picture plane is  $r_i(z) = G(z) \cos[\psi_i + 2\pi z[\lambda_i(1+z \sin \phi_i)]^{-1}]$ , where  $\phi_i$  describes the half-opening angle of the jet.
38. If  $\lambda^*$  is substantially different in one of the modes, it would indicate that either (i) the fitted wavelength of the mode has a large error, (ii) the mode has been identified incorrectly, or (iii) the mode does not grow at its resonant wavelength (for instance, if is driven externally or develops at a longer wavelength not exceeding the longest unstable wavelength).
39. The resulting basic relations are  $\lambda^* = [8R_j M_j \Gamma_j \sin \theta] / [1 + \eta^{0.5} \delta_j]$  and  $P_c = [(1+z)\lambda_j(1 + \eta^{0.5} \delta_j)] / [\beta_j \delta_j \sin \theta (1 + \eta^{0.5} \Gamma_j)]$ , where  $\delta_j = 1/[\Gamma_j(1 - \beta_j \sin \theta)]$  is the Doppler factor of the jet.
40. We thank P. E. Hardee and I. K. K. Pauliny-Toth for helpful discussions and comments on the manuscript. We gratefully acknowledge the VSOP Project, which is led by the Japanese Institute of Space and Astronomical Science in cooperation with many agencies, institutes, and observatories around the world. The National Radio Astronomy Observatory is a facility of the NSF operated under cooperative agreement by Associated Universities.

7 June 2001; accepted 24 August 2001

## Ferromagnetic Imprinting of Nuclear Spins in Semiconductors

R. K. Kawakami,<sup>1</sup> Y. Kato,<sup>1</sup> M. Hanson,<sup>2</sup> I. Malajovich,<sup>1</sup>  
J. M. Stephens,<sup>2</sup> E. Johnston-Halperin,<sup>1</sup> G. Salis,<sup>1</sup> A. C. Gossard,<sup>2</sup>  
D. D. Awschalom<sup>1\*</sup>

We examine how a ferromagnetic layer affects the coherent electron spin dynamics in a neighboring gallium arsenide semiconductor. Ultrafast optical pump-probe measurements reveal that the spin dynamics are unexpectedly dominated by hyperpolarized nuclear spins that align along the ferromagnet's magnetization. We find evidence that photoexcited carriers acquire spin-polarization from the ferromagnet, and dynamically polarize these nuclear spins. The resulting hyperfine fields are as high as 9000 gauss in small external fields (less than 1000 gauss), enabling ferromagnetic control of local electron spin coherence.

Investigations of electron spins in solids have led to several important discoveries such as giant magnetoresistance in metallic magnetic multilayers (1) and long spin-coherence times in semiconductors (~100 ns) (2). The recent development of layered ferromagnet/semiconductor heterostructures (3–7) enables integration of these approaches to spintronics, and presents new possibilities for controlling coherent electron spin dynamics in semiconductors through manipulation of the local magnetic environment. For instance, it is thought that effective magnetic fields generated by a ferromagnet could be exploited to change the quantum state of selected electron spins, while leaving others undisturbed (8).

To develop this type of “quantum magnetoelectronics” it is necessary to explore how such ferromagnetic layers affect the electron spin dynamics in nearby semiconductors.

We report that the electron spin dynamics in an *n*-type GaAs layer are strongly modified by an adjacent ferromagnetic layer. Unexpectedly, the dominant interaction is identified as hyperfine coupling with nuclear spins in GaAs (9–11), and not fringe fields or direct exchange interactions with the ferromagnet. To investigate the electron spin dynamics, we used the pump-probe technique of time-resolved Faraday rotation (TRFR) (12) to measure the precession of optically generated electron spins in a transverse magnetic field. Using the precession frequency as a sensitive magnetometer of the total field in the GaAs layer, we found that the ferromagnetic layer produces local fields as high as 9000 G in an applied field of 1000 G. These local fields follow the magnetic hysteresis loop of the ferromagnetic layer except near

zero applied field, where they vanish despite the presence of significant remanent magnetization. A series of measurements demonstrate that this local field arises from an unanticipated process: ferromagnetic imprinting of nuclear spins. In this carrier-mediated process, the ferromagnetic layer induces nuclear spin polarization in the adjacent GaAs layer along the local magnetization, leading to effective magnetic fields which act on the electron spins in GaAs through the hyperfine interaction (9). Thus, the dynamics of the optically generated electron spins can be controlled by a ferromagnet through the creation of a ferromagnetic imprint in the GaAs nuclear spin system.

Samples were grown by molecular beam epitaxy and had the following structure: ferromagnet/*n*-GaAs/Al<sub>0.75</sub>Ga<sub>0.25</sub>As/*n*<sup>+</sup>-GaAs(100) substrate. All layers up to the ferromagnet were grown in a separate chamber to maximize the optical quality of the 100-nm *n*-GaAs layer (Si:  $7 \times 10^{16} \text{ cm}^{-3}$ ). Four samples were prepared (13), each with a different ferromagnetic layer and Curie temperature  $T_C$ : 25-nm type-A MnAs ( $T_C \sim 320$  K) (3), 15-nm (Ga,Mn)As with ~5% Mn concentration ( $T_C \sim 75$  K) (4), five-period digital ferromagnetic heterostructure (DFH) of 1/2 monolayer (ML) MnAs spaced by 10 ML GaAs ( $T_C \sim 60$  K) (6), and 1/2 ML MnAs (henceforth termed “single layer”) ( $T_C \sim 55$  K) (6). The last three samples were capped with 20 ML of GaAs. We also prepared a control sample without a ferromagnetic layer. Each sample was mounted on fused silica with transparent epoxy and the substrates were removed up to the 400-nm AlGaAs layer by a selective etch (14).

The samples were placed inside a magneto-optical cryostat and electron spin dynamics in the GaAs layer were investigated by TRFR (12). Our pump-probe experiments used short

<sup>1</sup>Department of Physics and <sup>2</sup>Materials Department, University of California, Santa Barbara, CA 93106, USA.

\*To whom correspondence should be addressed. E-mail: awsch@physics.ucsb.edu